Particle Acceleration in Relativistic Plasma Turbulence

Luca Comisso* and Lorenzo Sironi†
Department of Astronomy and Columbia Astrophysics Laboratory, Columbia University, New York, New York 10027, USA

(Received 10 September 2018; revised manuscript received 14 November 2018; published 20 December 2018)

Due to its ubiquitous presence, turbulence is often invoked to explain the origin of nonthermal particles in astrophysical sources of high-energy emission. With particle-in-cell simulations, we study decaying turbulence in magnetically dominated (or, equivalently, "relativistic") pair plasmas. We find that the generation of a power-law particle energy spectrum is a generic by-product of relativistic turbulence. The power-law slope is harder for higher magnetizations and stronger turbulence levels. In large systems, the slope attains an asymptotic, system-size-independent value, while the high-energy spectral cutoff increases linearly with system size; both the slope and the cutoff do not depend on the dimensionality of our domain. By following a large sample of particles, we show that particle injection happens at reconnecting current sheets; the injected particles are then further accelerated by stochastic interactions with turbulent fluctuations. Our results have important implications for the origin of nonthermal particles in high-energy astrophysical sources.

DOI: 10.1103/PhysRevLett.121.255101

Despite decades of research [1–6], the origin of nonthermal particles in space and astrophysical systems remains poorly understood. Due to its ubiquitous presence, turbulence is often invoked as a promising source of accelerated particles [7–9], and significant progress has been made on both theoretical [10–14] and numerical [15–19] grounds. Turbulence is believed to play an important role in the energization of nonthermal particles in the solar corona and galaxy clusters [7–9], and it could also be important in magnetically dominated environments like pulsar magnetospheres and winds, jets from active galactic nuclei, and coronae of accretion disks [20–22]. Particle acceleration in magnetized turbulent flows might indeed power the bright nonthermal synchrotron and inverse Compton signatures from such high-energy sources [23–25].

While the turbulence dynamics in magnetically dominated ("relativistic") plasmas has been well characterized by fluid simulations [26–34], the process of particle acceleration can only be captured from first principles by means of fully kinetic particle-in-cell (PIC) codes. Pioneering studies of particle acceleration via driven turbulence in moderately magnetized pair plasmas [35] reported the generic development of nonthermal power-law distributions. However, the power-law tail was found to steepen with increasing system size, with disappointing implications for large-scale astrophysical sources. Here, by employing PIC simulations in unprecedentedly large domains, we show that the power-law slope reaches an asymptotic, system-size-independent value, with harder slopes for higher magnetizations and stronger turbulence levels. We show that particle injection happens at reconnecting current sheets; the injected particles are then further accelerated by stochastic interactions with turbulent fluctuations.

We solve the coupled Vlasov-Maxwell system of equations through the PIC method [36] employing the PIC code TRISTAN-MP [37,38] to perform 2D and 3D simulations of decaying turbulence in pair plasmas. The electron-positron plasma is initially uniform with density n_0 and follows a relativistic Maxwellian distribution with thermal spread $\theta_0 = k_B T_0/mc^2 = 0.3$. We set up a mean magnetic field $\langle \boldsymbol{B} \rangle = B_0 \hat{\boldsymbol{z}}$ and magnetic field fluctuations δB_x and δB_y, whose strength is parametrized by the magnetization $\sigma_0 = \delta B^2_{\rm rms0}/4\pi n_0 w_0 mc^2$, where $\delta B^2_{\rm rms0} = \langle \delta B^2 \rangle_{t=0}$, and $w_0 = \gamma_{th0} + \theta_0$ is the initial enthalpy per particle (γ_{th0} is the mean particle Lorentz factor). We vary σ_0 from 2.5 to 160 (i.e., in the magnetically dominated regime $\sigma_0 \gg 1$, where the Alfvén speed approaches the speed of light) and $\delta B_{\rm rms0}/B_0$ from 0.5 to 4. With our definition of σ_0, our results do not depend on the choice of initial thermal spread θ_0 (apart from an overall energy rescaling). We also define $\sigma_z = B_0^2/4\pi n_0 w_0 mc^2 = \sigma_0 (B_0^2/\delta B^2_{\rm rms0})$.

Turbulence develops from uncorrelated fluctuations with $\delta B_x = \sum_{m,n} \beta_{mn} n \sin(k_m x + \phi_{mn}) \cos(k_n y + \varphi_{mn})$ and $\delta B_y = -\sum_{m,n} \beta_{mn} m \cos(k_m x + \phi_{mn}) \sin(k_n y + \varphi_{mn})$, where $m, n \in \{1, \ldots, N\}$ are the mode numbers, $k_m = 2\pi m/L$ and $k_n = 2\pi n/L$ the wave numbers along x and y, respectively, ϕ_{mn} and φ_{mn} random phases, and $\beta_{mn} = 2\delta B_{\rm rms0}/[N(m^2+n^2)^{1/2}]$. With this choice, each (m, n) mode carries the same power, so the initial energy spectrum peaks near $k_N = 2\pi N/L$, where L is the domain size (typically, $N = 8$). This defines the energy-carrying scale $l = 2\pi/k_N$, used as our unit length. For 3D simulations, we also modulate δB_x and δB_y sinusoidally in the

z direction, with two modes of wavelength L and $L/2$ and random phases.

The large size of our computational domain (with L up to 65,600 cells in 2D and up to 2400 in 3D) allows us to achieve asymptotically converged results. The plasma skin depth $d_{e0} = c/\omega_{p0} = \sqrt{\gamma_{th0} mc^2/4\pi n_0 e^2}$ is resolved with 10 cells in 2D and 3 cells in 3D (in 2D we have checked that $d_{e0} = 3$ or 10 cells give identical results, including the development of turbulent structures). The simulation time step is controlled by the numerical speed of light of 0.45 cells/time step. We typically employ 16 (macro) particles per cell in 2D and 4 per cell in 3D, but we have tested that our results are the same when using more particles per cell (up to 256 in 2D and up to 16 in 3D).

Figure 1(a) shows the fully developed turbulent state from a 2D simulation with $\sigma_0 = 10$, by plotting the current density J_z. Vortexlike and sheetlike coherent structures are ubiquitous, in analogy to nonrelativistic kinetic simulations e.g., [39–43]. Elongated current sheets tend to fragment into chains of plasmoids due to the plasmoid instability [44–47]. As we show below, reconnecting current sheets—a natural byproduct of turbulent cascades in magnetized plasmas [48–52]—play a vital role for particle injection into the acceleration process. The time evolution of the magnetic power spectrum $P_B(k)$ is presented in Fig. 1(b). Each curve refers to a different time, as indicated by the corresponding vertical dashed lines in the inset, where we present the energy decay in turbulent fluctuations $\delta B^2_{\rm rms}/B^2_0$. As the magnetic energy decays, the inertial range ($kd_{e0} \lesssim 0.4$) of the magnetic power spectrum tends to flatten from $P_B(k) \propto k^{-5/3}$ [53,54] to $P_B(k) \propto k^{-3/2}$ [55,56]. At kinetic scales ($kd_{e0} \gtrsim 0.4$), the spectrum steepens to $P_B(k) \propto k^{-4}$, similar to what has been found in kinetic simulations of driven turbulence with moderate magnetizations [35,57].

The time evolution of the corresponding particle spectrum $dN/d\ln(\gamma - 1)$ is presented in Fig. 2(a), where γ is the particle Lorentz factor. The figure shows that efficient nonthermal particle acceleration is a self-consistent byproduct of relativistic turbulence. As a result of field dissipation, the spectrum shifts to energies much larger than the initial Maxwellian (shown by the blue line peaking at $\gamma - 1 \sim \gamma_{th0} - 1 \simeq 0.6$). At late times, when most of the turbulent energy has decayed, the spectrum stops evolving (orange and red lines): it peaks at $\gamma - 1 \sim \gamma_{th0}(1 + \sigma_0/2) - 1 \sim 5$, and extends well beyond the peak into a nonthermal tail of ultrarelativistic particles, with power-law slope $p = -d\log N/d\log(\gamma - 1) \sim 2.9$. The inset shows that the value of the power-law slope is not universal: for fixed $\delta B^2_{\rm rms0}/B^2_0$, the tail becomes harder with increasing σ_0, in agreement with Ref. [35] and in analogy to simulations of relativistic magnetic reconnection [58–62]; more dramatically, at fixed magnetization σ_0, the spectrum is much harder for stronger turbulent fluctuations (i.e., $\delta B^2_{\rm rms0}/B^2_0 \gtrsim 1$).

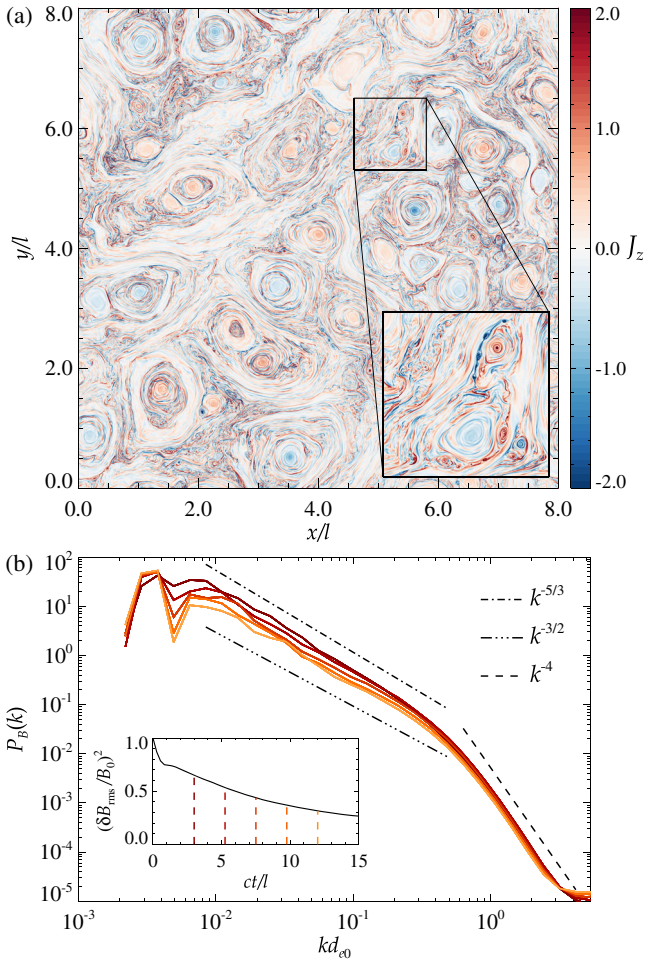

FIG. 1. Developed turbulence from a 2D simulation with $\sigma_0 = 10$, $\delta B_{\rm rms0}/B_0 = 1$, and $L/d_{e0} = 3280$ (with $l = L/8$). Top: Current density J_z at $ct/l = 5.5$ (normalized to en_0c) indicating the presence of coherent structures like current sheets, plasmoids, and vortices (see inset). Bottom: Magnetic power spectra computed at different times, as indicated by the vertical dashed lines (same color coding) in the inset, which also shows the time evolution of $\delta B^2_{\rm rms} = \langle \delta B^2 \rangle$ normalized to B^2_0.

The power-law slopes quoted in the inset of Fig. 2(a) persist in the limit of asymptotically large domains. In Fig. 2(b), we show for $\sigma_0 = 10$ and $\delta B^2_{\rm rms0}/B^2_0 = 1$ the dependence of the time-saturated particle spectrum on the size of our 2D box, which we vary in the range $L/d_{e0} \in \{410, 820, 1640, 3280, 6560\}$. While earlier works, which employed smaller domains, had claimed that the power-law slope steepens with increasing system size [35], we find that the slope saturates for asymptotically large systems [top inset in Fig. 2(b)], which allows us to extrapolate our results to the astrophysically relevant regime $L/d_{e0} \gg 1$. On the other hand, the high-energy cutoff γ_c—defined as the Lorentz factor where the spectrum drops one order of magnitude below the power-law best fit—linearly increases with system size [bottom inset in Fig. 2(b)]. As discussed below, stochastic acceleration by

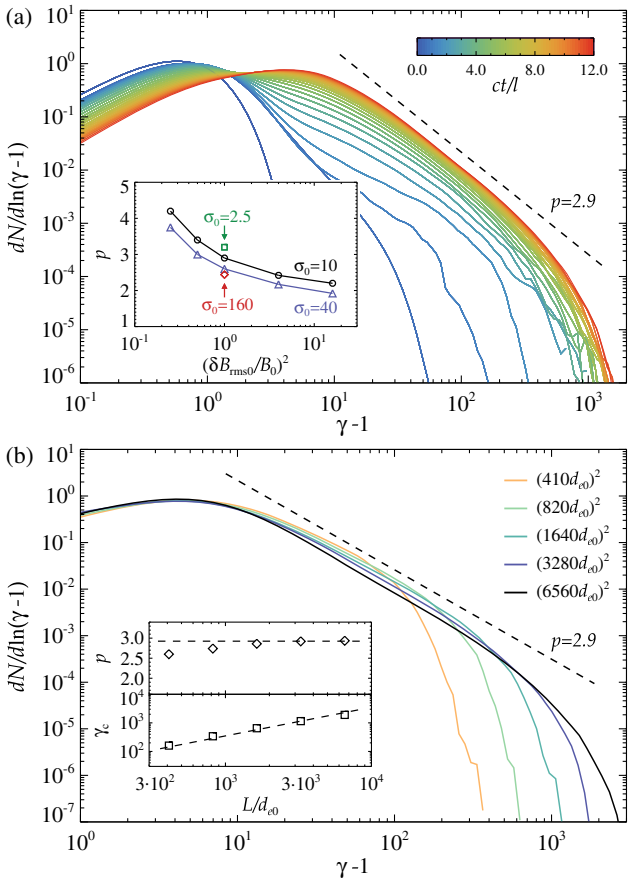

FIG. 2. Top: Particle spectrum evolution for the simulation in Fig. 1. At late times, the spectrum displays an extended power-law tail with slope $p = -d\log N/d\log(\gamma - 1) \sim 2.9$. The inset shows the dependence of p on $\delta B^2_{\rm rms0}/B^2_0$ and σ_0. Bottom: Particle spectra at late times ($ct/l = 12$) for simulations with fixed $\sigma_0 = 10$, $\delta B_{\rm rms0}/B_0 = 1$, and $l = L/8$, but different system sizes $L/d_{e0} \in \{410, 820, 1640, 3280, 6560\}$. The insets show the dependence of p (dashed line is the asymptotic slope $p = 2.9$) and the cutoff Lorentz factor γ_c [dashed line is the predicted scaling $\gamma_c \sim \sqrt{\sigma_z}\gamma_{th0}(l/d_{e0})$] on the system size.

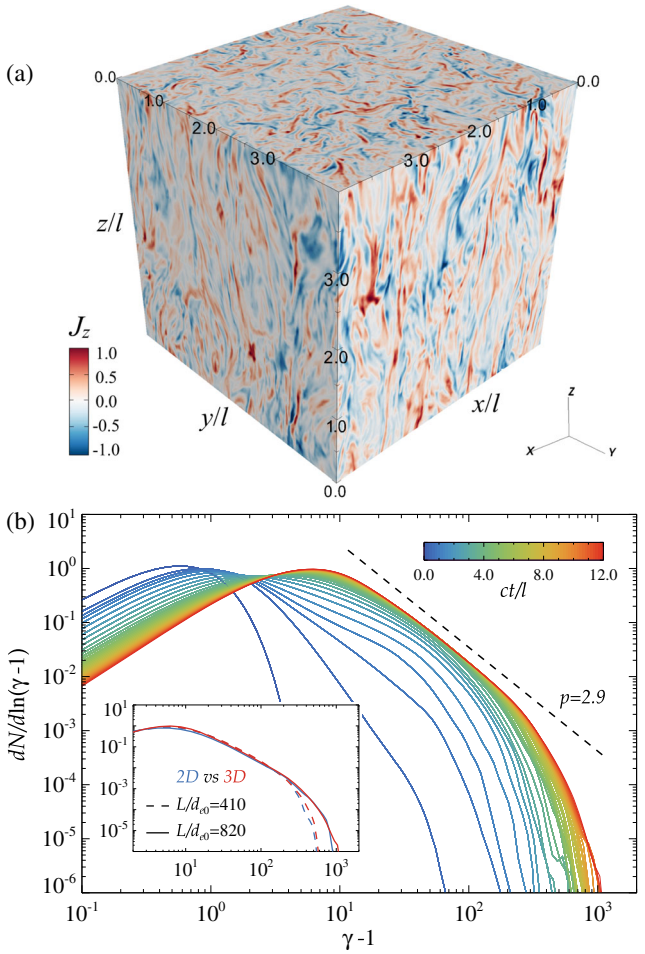

FIG. 3. Top: Current density J_z at $ct/l = 4$ from a 3D simulation with $\sigma_0 = 10$, $\delta B_{\rm rms0}/B_0 = 1$, $L/d_{e0} = 820$, and $l = L/4$, showing the copious presence of current sheets. Bottom: Time evolution of the corresponding particle spectrum. The inset shows for two different box sizes that the time-saturated particle spectra are almost identical between 2D (blue) and 3D (red).

turbulent fluctuations dominates the energy gain of nonthermal particles. High-energy particles cease to be efficiently scattered by turbulent fluctuations when their gyroradius exceeds the energy-carrying scale $l = 2\pi/k_N$, implying an upper limit to their Lorentz factor of $\gamma_c \sim e\sqrt{\langle B^2\rangle}l/mc^2 \sim \sqrt{\sigma_z}\gamma_{th0}(l/d_{e0})$, which successfully matches the scaling of γ_c on system size in the inset of Fig. 2(b) (this argument assumes that turbulence survives long enough to allow the particles to reach this upper limit). By varying l/L, we have explicitly verified that $\gamma_c \propto l$, rather than $\gamma_c \propto L$.

We have confirmed our main results with large-scale 3D simulations, since several properties of the turbulence itself, as the energy decay rate and the degree of intermittency, are known to be sensitive to dimensionality [53]. Results from our largest 3D simulation are presented in Fig. 3. The plot of J_z in the fully developed turbulent state (top) shows the presence of a multitude of current sheets, as found in 2D. The particle energy spectrum evolution is presented in Fig. 3(b). A pronounced nonthermal tail develops, whose power-law slope and high-energy cutoff are remarkably identical to its 2D counterpart (in the inset, we compare the time-saturated spectra of 2D and 3D simulations for two different box sizes, which nearly overlap).

To unveil the particle acceleration mechanisms, we have tracked the trajectories of a random sample of $\sim 10^6$ particles from a 2D simulation with $\sigma_0 = 10$, $\delta B_{\rm rms0}/B_0 = 1$, and $L/d_{e0} = 1640$. In Fig. 4(a) we show the Lorentz factor evolution of 10 particles that eventually populate the nonthermal tail [i.e., with $\gamma > 30$ at $ct/l = 12$, compare with the cyan line in Fig. 2(b)]. A common feature of these tracks is the rapid energy increase from $\gamma \sim \gamma_{th0}$ up to $\gamma \sim 10$–100. Indeed, we have verified that the overwhelming majority

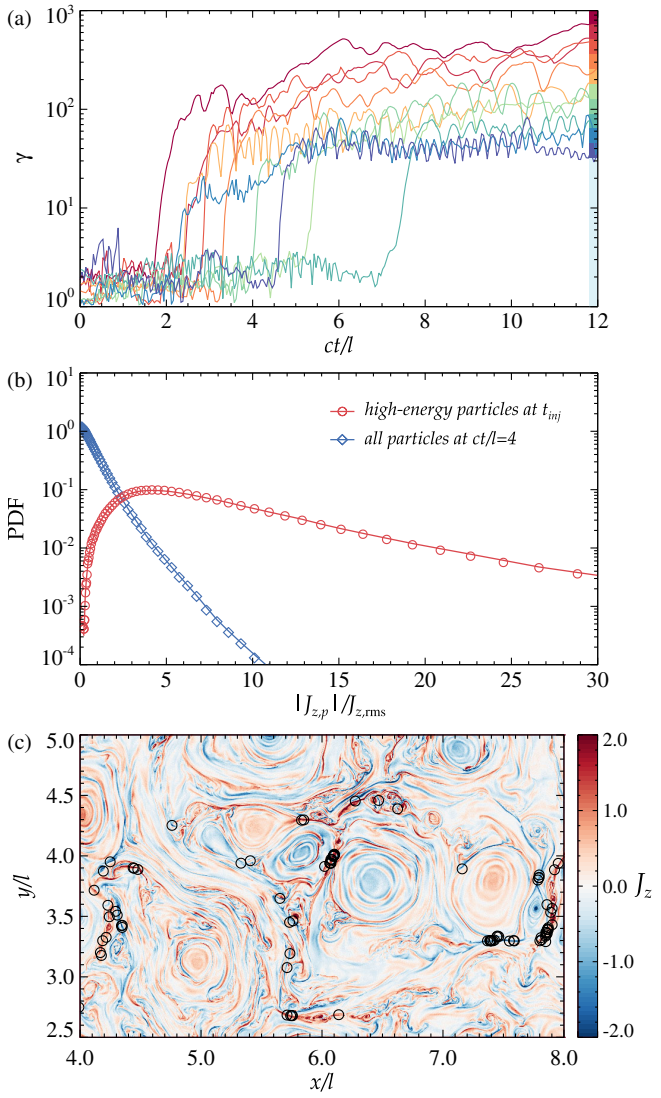

FIG. 4. Top: Evolution of the Lorentz factor for 10 representative particles selected to end up in different energy bins at $ct/l = 12$ (matching the different colors in the colorbar on the right). Middle: PDFs of $|J_{z,p}|/J_{z,\rm rms}$ experienced by the injected particles at their $t_{\rm inj}$ (red circles) and by all tracked particles at $ct/l = 4$ (blue diamonds). Bottom: Zoom of J_z at $ct/l = 4$ with circles indicating the positions of the particles that are injected around this time.

(∼97%) of the particles belonging to the nonthermal tail experience in their life such a sudden episode of energy gain. This event is extracting the particles from the thermal pool and injecting them into the acceleration process. Inspired by Fig. 4(a), we identify the injection time $t_{\rm inj}$ as the time when the energy increase rate (averaged over $\Delta t = 45 d_{e0}/c$) satisfies $\Delta\gamma/\Delta t > \dot{\gamma}_{thr}$, and prior to this time the particle Lorentz factor was $\gamma < 4\gamma_{th0} \sim 6$. We take $\dot{\gamma}_{thr} \simeq 0.01\sqrt{\sigma_0}\gamma_{th0}\omega_{p0}$, but we have verified that our identification of $t_{\rm inj}$ is nearly the same when varying $\dot{\gamma}_{thr}$ around this value by up to a factor of 3.

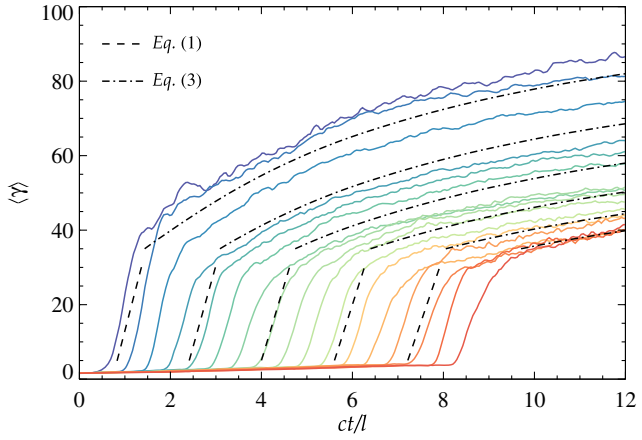

FIG. 5. Evolution of the mean Lorentz factor of different generations of particles. The initial energy gain, due to the reconnection electric field, can be modeled as in Eq. (1) with $\beta_R = 0.05$ (dashed lines), while the subsequent evolution, governed by stochastic interactions with the turbulent fluctuations, follows Eq. (3) (dot-dashed line).

We then explore the properties of the electromagnetic fields at the injection location. The red circles in Fig. 4(b) show the probability density function (PDF) of the electric current density $|J_{z,p}|$ experienced by the particles at their injection time (normalized by $J_{z,\rm rms}$ in the whole domain at that time). The peak of the PDF is at $|J_{z,p}| \sim 4J_{z,\rm rms}$, and ∼95% of the injected particles reside at $|J_{z,p}| > 2J_{z,\rm rms}$, a threshold that is usually employed to identify current sheets [63]. This should be contrasted with the blue diamonds, showing the PDF of the electric current experienced by all tracked particles at $ct/l = 4$, regardless of whether they are injected or not. As expected, this peaks at zero, and only ∼9% of particles have $|J_{z,p}| > 2J_{z,\rm rms}$. Thus, particle injection into the acceleration process occurs at current sheets, more specifically, at reconnecting current sheets. This is illustrated in Fig. 4(c), where we show J_z/en_0c in a subset of the simulation domain at $ct/l = 4$. The overplotted black circles indicate the locations of particles whose $t_{\rm inj}$ is around this time. Clearly, most of the particles participating in the injection episode reside at active reconnection layers, fragmenting into plasmoids.

Acceleration by the reconnection electric field [58–60] governs the first phase of particle energization, as shown in Fig. 5. Here, each colored curve represents the average Lorentz factor of particles having the same injection time $t_{\rm inj}$ (within $\Delta t_{\rm inj} = 0.48ct/l$). The linear growth from $\langle\gamma\rangle \sim 1$ up to $\langle\gamma\rangle \sim 30$ (i.e., the injection phase) is powered by field-aligned electric fields, whose magnitude is $|E_\parallel| \simeq \beta_R \delta B_{\rm rms}$, via

$$\frac{d\langle\gamma\rangle}{dt} = \beta_R \frac{\delta B_{\rm rms}}{B_0}\sqrt{\sigma_z(1+\theta_0/\gamma_{th0})}\gamma_{th0}\omega_{p0}. \quad (1)$$

The dashed black lines in Fig. 5 show the predictions of Eq. (1) assuming a reconnection rate $\beta_R \simeq 0.05$, as

appropriate for relativistic reconnection with guide field comparable to the alternating field [64].

After the injection phase, the subsequent energy gain (which eventually dominates the overall energization of highly nonthermal particles) is powered by perpendicular electric fields via stochastic scatterings off the turbulent fluctuations. This is a biased random walk in momentum space, which can be modeled with a Fokker-Planck approach [65], provided that the fractional momentum change in single scatterings is small, as it is the case in our simulations. From the Fokker-Planck equation for relativistic particles,

$$\frac{d\langle\gamma\rangle}{dt} = \frac{1}{\gamma^2}\frac{\partial}{\partial\gamma}[\gamma^2 D_p], \qquad D_p = \frac{1}{3}\frac{\delta V_{\rm rms}^2}{c}\frac{\gamma^2}{\lambda_{\rm mfp}(\gamma)}, \qquad (2)$$

where D_p is the diffusion coefficient in momentum space for a stochastic process akin to the second-order Fermi mechanism, $\delta V_{\rm rms}$ is the typical velocity of the scatterers (typically $\delta V_{\rm rms}/c \lesssim 0.3$ in our simulations, which justifies a nonrelativistic treatment), and $\lambda_{\rm mfp}(\gamma)$ is the particle mean-free path. Since particles are most efficiently scattered by turbulent fluctuations on the scale of their gyroradius [66], we assume a Bohm-like scaling for $\lambda_{\rm mfp}(\gamma) = \kappa(c/\omega_c)(B_0/\delta B_{\rm rms})^2$ where $\omega_c = eB_0/\gamma mc$ is the gyrofrequency and κ is a dimensionless coefficient. This leads to

$$\frac{d\langle\gamma\rangle}{dt} = \kappa^{-1}\frac{\delta B_{\rm rms}^2}{B_0^2}\frac{\delta V_{\rm rms}^2}{c^2}\sqrt{\sigma_z(1+\theta_0/\gamma_{th0})}\gamma_{th0}\omega_{p0}. \qquad (3)$$

Taking the temporal decay of the magnetic and velocity fluctuations directly from our simulation, we obtain for $\kappa = 10$ the dot-dashed lines in Fig. 5, which agree well with our simulation results.

In summary, we have demonstrated that relativistic plasma turbulence is a viable mechanism for particle acceleration, since it self-consistently generates nonthermal power-law tails. The power-law slope is harder (near $p \sim 2$) for higher magnetizations and stronger turbulence levels. Thanks to our large domains, we have demonstrated that the power-law slope reaches an asymptotic, system-size-independent value, while the high-energy spectral cutoff increases linearly with system size; this allows us to extrapolate our results to the macroscopic scales of astrophysical sources. The time-saturated particle energy spectrum is remarkably similar in 2D and 3D, suggesting that the same acceleration process operates, regardless of the dimensionality. By following a large sample of particles, we have shown that their energization occurs in two stages: particle injection happens at reconnecting current sheets; this is followed by a phase of stochastic acceleration where the particles scatter off turbulent fluctuations. Analytical predictions are in agreement with the simulations results, confirming the two-stage nature of the acceleration process.

It is a pleasure to acknowledge fruitful discussions with Mikhail Medvedev, Jonathan Zrake, Vahé Petrosian, Chuanfei Dong, Yi-Min Huang, Maxim Lyutikov, Vassilis Tsiolis, and Loukas Vlahos. This research acknowledges support from DoE DE-SC0016542, NASA Fermi NNX-16AR75G, NASA ATP NNX-17AG21G, and NSF ACI-1657507. The simulations were performed on Habanero at Columbia, on NASA (Pleiades) and NERSC (Edison) resources.

*luca.comisso@columbia.edu
†lsironi@astro.columbia.edu

[1] E. Fermi, Phys. Rev. **75**, 1169 (1949).
[2] E. N. Parker and D. A. Tidman, Phys. Rev. **111**, 1206 (1958).
[3] P. A. Sturrock, Phys. Rev. **141**, 186 (1966).
[4] R. M. Kulsrud and A. Ferrari, Astrophys. Space Sci. **12**, 302 (1971).
[5] A. R. Bell, Mon. Not. R. Astron. Soc. **182**, 147 (1978).
[6] R. D. Blandford and J. P. Ostriker, Astrophys. J. **221**, L29 (1978).
[7] D. B. Melrose, *Plasma Astrohysics. Nonthermal Processes in Diffuse Magnetized Plasmas* (Gordon and Breach, New York, 1980).
[8] V. Petrosian, Space Sci. Rev. **173**, 535 (2012).
[9] A. Lazarian, L. Vlahos, G. Kowal, H. Yan, A. Beresnyak, and E. de Gouveia Dal Pino, Space Sci. Rev. **173**, 557 (2012).
[10] J. M. Pryadko and V. Petrosian, Astrophys. J. **482**, 774 (1997).
[11] R. Schlickeiser and J. A. Miller, Astrophys. J. **492**, 352 (1998).
[12] B. D. G. Chandran, Phys. Rev. Lett. **85**, 4656 (2000).
[13] G. Brunetti and A. Lazarian, Mon. Not. R. Astron. Soc. **378**, 245 (2007).
[14] J. W. Lynn, E. Quataert, B. D. G. Chandran, and I. J. Parrish, Astrophys. J. **791**, 71 (2014).
[15] W. H. Matthaeus, J. J. Ambrosiano, and M. L. Goldstein, Phys. Rev. Lett. **53**, 1449 (1984).
[16] P. Dmitruk, W. H. Matthaeus, and N. Seenu, Astrophys. J. **617**, 667 (2004).
[17] S. Dalena, A. F. Rappazzo, P. Dmitruk, A. Greco, and W. H. Matthaeus, Astrophys. J. **783**, 143 (2014).
[18] Y. Matsumoto, T. Amano, T. N. Kato, and M. Hoshino, Science **347**, 974 (2015).
[19] H. Isliker, L. Vlahos, and D. Constantinescu, Phys. Rev. Lett. **119**, 045101 (2017).
[20] M. Lyutikov, T. Temim, S. Komissarov, P. Slane, L. Sironi, and L. Comisso, arXiv:1811.01767.
[21] L. Chen, Astrophys. J. Suppl. Ser. **235**, 39 (2018).
[22] A. M. Beloborodov, Astrophys. J. **850**, 141 (2017).
[23] M. C. Begelman, R. D. Blandford, and M. J. Rees, Rev. Mod. Phys. **56**, 255 (1984).
[24] F. Yuan and R. Narayan, Annu. Rev. Astron. Astrophys. **52**, 529 (2014).
[25] R. Bühler and R. Blandford, Rep. Prog. Phys. **77**, 066901 (2014).
[26] J. Cho, Astrophys. J. **621**, 324 (2005).

[27] T. Inoue, K. Asano, and K. Ioka, Astrophys. J. **734**, 77 (2011).
[28] J. Zrake and A. I. MacFadyen, Astrophys. J. **744**, 32 (2012).
[29] J. Zrake and A. I. MacFadyen, Astrophys. J. Lett. **763**, L12 (2013).
[30] J. Cho and A. Lazarian, Astrophys. J. **780**, 30 (2014).
[31] J. Zrake, Astrophys. J. Lett. **794**, L26 (2014).
[32] M. Takamoto and A. Lazarian, Astrophys. J. Lett. **831**, L11 (2016).
[33] J. Zrake and W. E. East, Astrophys. J. **817**, 89 (2016).
[34] M. Takamoto and A. Lazarian, Mon. Not. R. Astron. Soc. **472**, 4542 (2017).
[35] V. Zhdankin, G. R. Werner, D. A. Uzdensky, and M. C. Begelman, Phys. Rev. Lett. **118**, 055103 (2017).
[36] C. K. Birdsall and B. Langdon, *Plasma Physics via Computer Simulation* (McGraw-Hill, New York, 1985).
[37] O. Buneman, in *Computer Space Plasma Physics: Simulation Techniques and Software*, edited by H. Matsumoto and Y. Omura (Terra Scientific, Tokyo, 1993).
[38] A. Spitkovsky, AIP Conf. Proc. **801**, 345 (2005).
[39] S. Servidio, F. Valentini, F. Califano, and P. Veltri, Phys. Rev. Lett. **108**, 045001 (2012).
[40] M. Wan, W. H. Matthaeus, H. Karimabadi, V. Roytershteyn, M. Shay, P. Wu, W. Daughton, B. Loring, and S. C. Chapman, Phys. Rev. Lett. **109**, 195001 (2012).
[41] J. M. TenBarge and G. G. Howes, Astrophys. J. Lett. **771**, L27 (2013).
[42] L. Franci, S. Landi, L. Matteini, A. Verdini, and P. Hellinger, Astrophys. J. **812**, 21 (2015).
[43] K. D. Makwana, V. Zhdankin, H. Li, W. Daughton, and F. Cattaneo, Phys. Plasmas **22**, 042902 (2015).
[44] L. Comisso, M. Lingam, Y.-M. Huang, and A. Bhattacharjee, Phys. Plasmas **23**, 100702 (2016).
[45] Y.-M. Huang, L. Comisso, and A. Bhattacharjee, Astrophys. J. **849**, 75 (2017).
[46] T. Tajima and K. Shibata, *Plasma Astrophysics* (Addison-Wesley, Reading, MA, 1997).
[47] N. F. Loureiro, A. A. Schekochihin, and S. C. Cowley, Phys. Plasmas **14**, 100703 (2007).
[48] V. Carbone, P. Veltri, and A. Mangeney, Phys. Fluids A **2**, 1487 (1990).
[49] A. Mallet, A. A. Schekochihin, and B. D. G. Chandran, Mon. Not. R. Astron. Soc. **468**, 4862 (2017).
[50] N. F. Loureiro and S. Boldyrev, Phys. Rev. Lett. **118**, 245101 (2017).
[51] L. Comisso, Y.-M. Huang, M. Lingam, E. Hirvijoki, and A. Bhattacharjee, Astrophys. J. **854**, 103 (2018).
[52] C. Dong, L. Wang, Y.-M. Huang, L. Comisso, and A. Bhattacharjee, Phys. Rev. Lett. **121**, 165101 (2018).
[53] D. Biskamp, *Magnetohydrodynamic Turbulence* (Cambridge University Press, Cambridge, England, 2003).
[54] C. Thompson and O. Blaes, Phys. Rev. D **57**, 3219 (1998).
[55] P. S. Iroshnikov, Astron. Zh. **40**, 742 (1963).
[56] R. H. Kraichnan, Phys. Fluids **8**, 1385 (1965).
[57] V. Zhdankin, G. R. Werner, D. A. Uzdensky, and M. C. Begelman, Astrophys. J. Lett. **867**, L18 (2018).
[58] L. Sironi and A. Spitkovsky, Astrophys. J. Lett. **783**, L21 (2014).
[59] F. Guo, H. Li, W. Daughton, and Y.-H. Liu, Phys. Rev. Lett. **113**, 155005 (2014).
[60] G. R. Werner, D. A. Uzdensky, B. Cerutti, K. Nalewajko, and M. C. Begelman, Astrophys. J. Lett. **816**, L8 (2016).
[61] M. Lyutikov, L. Sironi, S. S. Komissarov, and O. Porth, J. Plasma Phys. **83**, 635830602 (2017).
[62] M. Petropoulou and L. Sironi, Mon. Not. R. Astron. Soc. **481**, 5687 (2018).
[63] A. F. Rappazzo, W. H. Matthaeus, D. Ruffolo, M. Velli, and S. Servidio, Astrophys. J. **844**, 87 (2017).
[64] G. R. Werner and D. A. Uzdensky, Astrophys. J. Lett. **843**, L27 (2017).
[65] R. Blandford and D. Eichler, Phys. Rep. **154**, 1 (1987).
[66] Stochastic acceleration occurs when the gyroradius is large, thus averaging out small scale fluctuations or noise on grid scales.